Photo-Induced Holes Initiating Peroxymonosulfate Oxidation for Carbamazepine Degradation via Singlet Oxygen

Yifei Qi [1], **Xiaoyue Zhou** [1], **Zhenjie Li** [1], **Renli Yin** [1,*], **Junhao Qin** [1], **Huashou Li** [1], **Wanqian Guo** [2], **Adela Jing Li** [1,*] and **Rongliang Qiu** [1]

1   Guangdong Provincial Key Laboratory of Agricultural & Rural Pollution Abatement and Environmental Safety, College of Natural Resources and Environment, South China Agricultural University, Guangzhou 510642, China

2   State Key Laboratory of Urban Water Resource and Environment, School of Environment, Harbin Institute of Technology, Harbin 150090, China

*   Correspondence: yinrenli@scau.edu.cn (R.Y.); jing.li@scau.edu.cn (A.J.L.)

Abstract: Peroxymonosulfate (PMS) has been intensively used to enhance the photocatalytic activity of catalysts, which is adopted as an electron acceptor to inhibit the recombination of electrons and holes. However, the effect of holes generated by visible light (VL) on PMS activation is always overlooked. Herein, the $VL/Bi_2WO_6/PMS$ process was constructed for the efficient removal of organics, in which the degradation rate of carbamazepine (CBZ) increased by over 33.0 times by the introduction of PMS into Bi_2WO_6 under visible light. The radical quenching and determination experiments confirmed that the photogenerated holes could firstly oxidize PMS to form $SO_5^{\bullet-}$ and react with HSO_5^- to produce $^1O_2$, then inducing the formation of other reactive species to greatly enhance the performance of pollutant removal by the $VL/Bi_2WO_6/PMS$ process. Density functional theory (DFT) predicted that sites with high Fukui index (f^0) on CBZ were more susceptible to being attacked, resulting in hydroxylation, ring closure, and C=C bond cleavage of CBZ. Toxicity estimation indicated that photocatalysis degradation products from CBZ were less toxic compared to the parent compound. This study provides a potential avenue for improving photocatalytic efficiency and widening the application of photocatalytic technology in wastewater purification.

Keywords: Bi_2WO_6; carbamazepine; peroxymonosulfate; photocatalysis; singlet oxygen

1. Introduction

The freshwater crisis is exacerbated by severe water pollution, including naturally occurring contaminants and synthetic chemicals. Pharmaceuticals and personal care products (PPCPs), a unique group of emerging environmental contaminants, have been seriously detected in water systems, endangering human health and causing ecological problems [1,2]. Therefore, developing effective technology to realize the efficient removal of PPCPs is still an urgent task.

Photocatalysis is a green and effective water treatment technology [3–5] that has attracted widespread attention due to its stability and excellent degradation efficiency [6]. Reports have demonstrated that photocatalytic processes can quantitatively and rapidly break down organic non-degradable pollutants into CO_2 and other harmless small molecules without the need for chemical oxidants such as H_2O_2 and O_3 [7–9]. As a renewable-energy-source-driven technology, semiconductor photocatalytic processes can effectively remove organic compounds [10–12]. Compared with other photocatalysts, the similar and specific crystal phase of Bi_aAO_b ensures superior electron transport capability [13]. Among these semiconductors, Bi_2WO_6, composed of accumulated perovskite-type $(Bi_2O_2)^{2+}$ and $(WO_4)^{2-}$ octahedral layers [14], have drawn extensive attention owing to their excellent visible light absorption, low cost, nontoxicity, suitable band potential, and high chemical stability [13,15–17]. Especially, the unique layered structure and intrinsic electric field, with

superior physical and chemical properties of suitable band gap (2.8 eV), suitable electrical and photostability, catalytic behavior, and nontoxicity, can facilitate the migration of photogenerated carriers [15,17–20]. Therefore, Bi_2WO_6 is considered a potential candidate for photocatalysts with suitable photocatalytic activity [21,22]. However, the application of Bi_2WO_6 in photocatalytic systems for actual wastewater treatment is very limited. The most critical drawback might be due to the high recombination rate of photogenerated carriers and low photoconversion efficiency, thus resulting in the limited production of reactive oxide species (ROS) [23–25].

Notwithstanding such shortage, the introduction of peroxymonosulfate (PMS) has recently been adopted as an efficient strategy to inhibit recombination and promote photoconversion efficiency for boosting photocatalytic activity under visible light illumination [26]. PMS is always known as an electron acceptor in photocatalysis to reduce the recombination of e_{cb}^- and h_{vb}^+ [27], accompanied by PMS activation by the accepted electrons to generate other reactive oxidative species (ROS) (•OH, $SO_4^{•-}$, etc.) to enhance the photocatalytic capacity for organics decomposition [28–30]. On the other hand, the photogenerated holes have a higher oxidation potential than PMS [31]; thus, PMS is also expected to act as an electron donor to be oxidized by holes to generate multifunctional ROS. However, the effect of the photogenerated holes on PMS activation in photocatalytic systems is always overlooked.

Herein, carbamazepine (CBZ), a commonly used and largely residual detected pharmaceutical, was chosen as the target pollutant to test the oxidation capacity of the photocatalytic PMS activation by Bi_2WO_6. The degradation performance of CBZ by the $VL/Bi_2WO_6/PMS$ process was firstly evaluated through comparative studies. Then the different activation mechanism of PMS in the $VL/Bi_2WO_6/PMS$ process was further analyzed by the quenching and EPR experiments, in which the photogenerated holes initiate PMS oxidation to generate singlet oxygen that contributes to the efficient removal of CBZ. Finally, the oxidative paths of CBZ were derived by the combination of experimental determination and theoretical density functional theory (DFT), while the acute toxicity of products was further estimated to illustrate the suitability of the $VL/Bi_2WO_6/PMS$ process for wastewater treatment.

2. Results and Discussion

2.1. Characterization of Bi_2WO_6

In order to study its crystallinity and purity, the XRD patterns of the prepared photocatalysts were recorded. As shown in Figure 1a, it can be observed that diffraction peaks at $2\theta = 23.0°, 28.2°, 32.9°, 47.0°, 55.9°, 58.6°, 68.8°, 76.0°$, and $78.3°$ were obvious in pure Bi_2WO_6. These typically peaks can be indexed to (130), (131), (200), (260), (331), (1,10,0), (2,10,1), (333), and (204) crystal planes of orthorhombic crystal of Bi_2WO_6 (PDF#79-2381), respectively. The morphologies of as-synthesized Bi_2WO_6 have been characterized. For the SEM image of pure Bi_2WO_6 (Figure 1b), it is observed that the structures of 3D flowers are stacked together and uniformly distributed, of which the type was reported to be favorable with photocatalytic effect [15]. The SEM image in Figure 1c presents the morphology of pure Bi_2WO_6 as microspheres. This structure is in agreement with the results presented in the TEM images (Figure 1d).

The chemical surface states of Bi_2WO_6 samples were revealed by XPS analysis. As can be seen from Figure S1, the sample is composed of Bi, W, O. The high-resolution spectra of Bi 4 f, W 4 f, and O 1 s are shown in Figure S1. All binding energies were calibrated using the binding energy of C 1 s. The peaks at 158.89 eV and 164.18 eV contribute to 4 $f_{7/2}$ and 4 $f_{5/2}$ of Bi^{3+} in Bi_2WO_6, respectively (Figure S1b). For the W 4f XPS spectrum (Figure S1c), the two characteristic peaks at 35.16 eV and 37.36 eV are consistent with W 4 $f_{7/2}$ and W 4 $f_{5/2}$, indicating that the W element is present in the W^{6+} state. From the XPS spectrum of the O 1s of Bi_2WO_6 (Figure S1d), a strong peak is observed at 530.06 eV corresponding to the O 1s of Bi_2WO_6. The above characterization initially confirmed the successful synthesis of bismuth tungstate and showed the potential of photocatalysis.
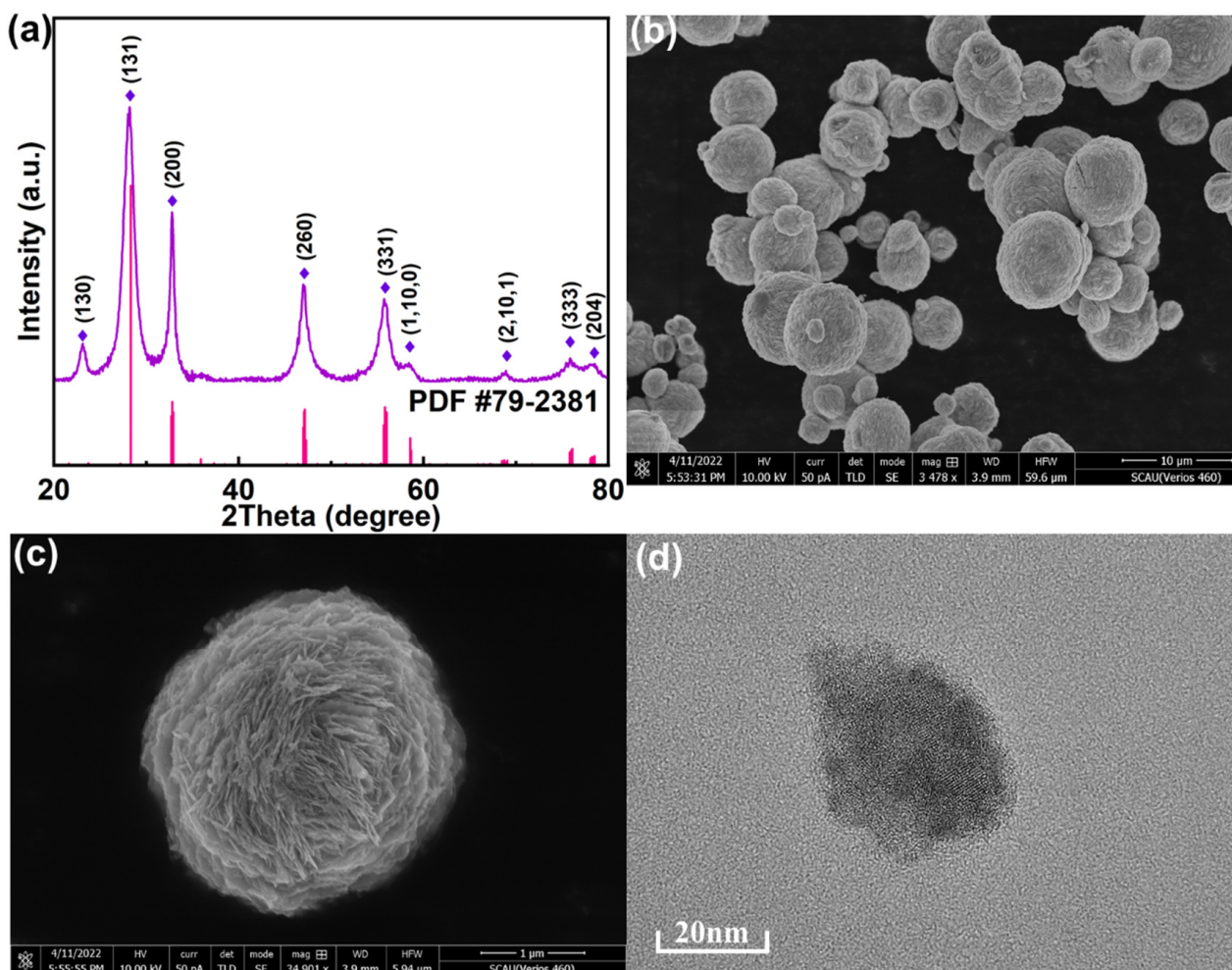
Figure 1. Typical XRD pattern (**a**), FESEM micrographs of Bi_2WO_6 flower core-structure (**b**,**c**), and TEM images of Bi_2WO_6 (**d**).

2.2. Performance of CBZ Degradation in the VL/Bi_2WO_6/PMS Process

In this study, the performance of the VL/Bi_2WO_6/PMS system for CBZ degradation was comparatively observed. The oxidation capacity of VL and PMS on CBZ was negligible, while the adsorption capacity of Bi_2WO_6 was limited (less than 2% for 2 h, Figure 2a). Furthermore, the activation ability of VL and Bi_2WO_6 for PMS on CBZ degradation is negligible, respectively (VL/PMS and Bi_2WO_6/PMS process, Figure 2a). The degradation of CBZ by photocatalysis of VL/Bi_2WO_6 was also insignificant, and the removal rate of CBZ at 2 h was only 5.0%. It is worth noting that the rate of CBZ degradation in the VL/Bi_2WO_6/PMS system is much higher than that of all other systems, which is also much higher than the sum of all other systems. Comparing the capacity and rate of CBZ degradation in VL/Bi_2WO_6 system with that in VL/Bi_2WO_6/PMS system, the introduction of PMS greatly enhanced the catalytic ability of Bi_2WO_6 for photocatalysis to remove pollutants.

Furthermore, the rate constants of the VL/Bi_2WO_6/PMS, Bi_2WO_6/PMS, and VL/Bi_2WO_6 processes were observed by pseudo-first-order kinetic monitoring. Figure 2b shows that the combined VL/Bi_2WO_6/PMS process degrades CBZ at a rate constant 16.4 and 32.8 times higher than the Bi_2WO_6/PMS and VL/Bi_2WO_6 photocatalytic processes, respectively. According to the above results, Bi_2WO_6 material shows limited photocatalytic capacity under visible light, while the introduction of PMS can greatly improve its photocatalytic ability. In addition, solely visible light irradiation and Bi_2WO_6 showed little contribution to PMS

activation; thus, the efficient activation of PMS in the VL/Bi$_2$WO$_6$/PMS system was due to the combined effect of photocatalytic VL/Bi$_2$WO$_6$ process. Therefore, PMS can inhibit electron recombination with holes of the VL/Bi$_2$WO$_6$/PMS system to promote the photocatalytic capacity of Bi$_2$WO$_6$, in which the photocatalysis of Bi$_2$WO$_6$ initiates the activation of PMS to generate radicals, thereby further improving the removal performance of the combined process. However, that the PMS activation is initiated by the photogenerated electron or hole is unclear and overlooked before.
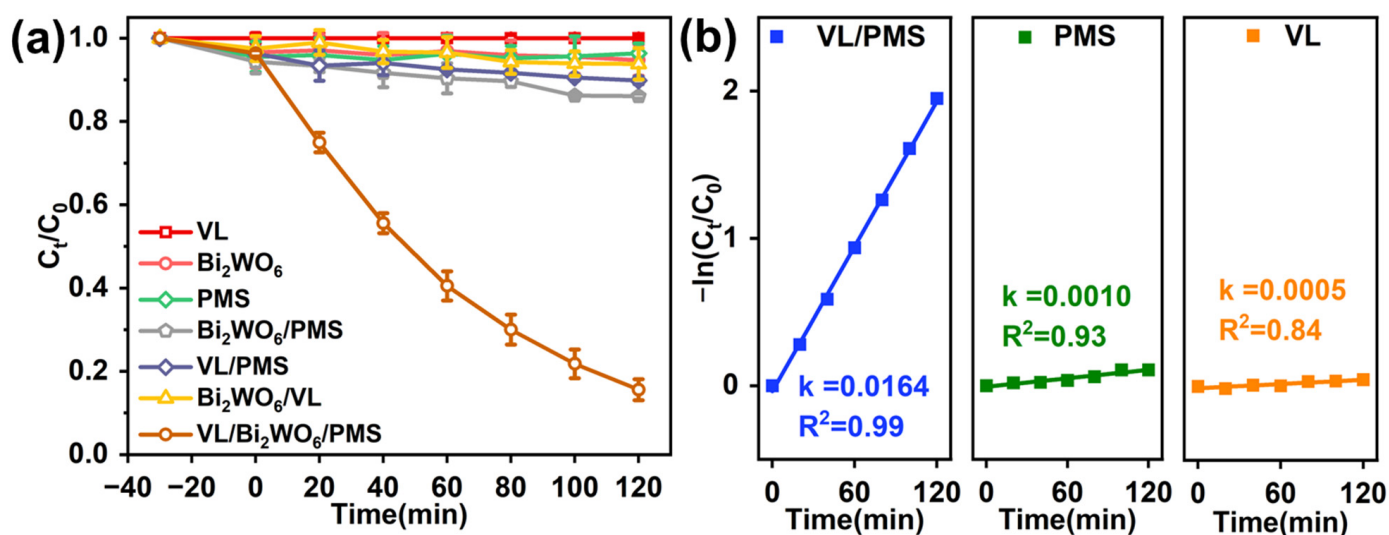

Figure 2. CBZ degradation performance under different comparative oxidation processes (**a**) and the rate constants of different cases with Bi$_2$WO$_6$ (**b**). Experimental conditions: LI = 200 mW cm^{-2}, Bi$_2$WO$_6$ dosage = 1.0 g L^{-1}, [PMS]$_0$ = 0.50 g L^{-1}, [CBZ] = 10 mg L^{-1}, pH = 7.0, and T = 25 °C.

2.3. Activation Mechanism in the VL/Bi$_2$WO$_6$/PMS System

To elucidate the mechanism of PMS activation by photocatalytic Bi$_2$WO$_6$ process, quenching experiments of ROS were performed. Accordingly, •OH and SO$_4$$^{•-}$, •O$_2$$^-$, •OH, e$^-$, ^{1}O$_2$, and h$^+$ were scavenged with MeOH, p-BQ, TBA, K$_2$Cr$_2$O$_7$, FFA, and EDTA, respectively [25,32–34] The previous step elucidated that the efficient activation of PMS in the VL/Bi$_2$WO$_6$/PMS process was due to the photocatalytic VL/Bi$_2$WO$_6$ system. Thus, the photogenerated electrons and holes might play important roles in PMS activation. As shown in Figure 3a, when EDTA (h$^+$ scavenger) was added to the reaction system, the k-values decreased by 98%, while the addition of K$_2$Cr$_2$O$_7$ (e$^-$ scavenger) increased the degradation rate of CBZ by 14%, respectively. It was indicated that the h$^+$ played a key role in PMS activation in the VL/Bi$_2$WO$_6$/PMS process. The enhancement of K$_2$Cr$_2$O$_7$ might be attributed to the scavenging of electrons to release more holes for PMS activation. Thus, in the VL/Bi$_2$WO$_6$/PMS system, it is the photogenerated hole that initiates PMS activation rather than the generated electrons. In addition, the scavenging results showed that the CBZ degradation rate of organic pollutants was also inhibited by MeOH addition under the same molar ratio of TBA, indicating the generation of •OH, SO$_4$$^{•-}$ and •O$_2$$^-$ also contributed to CBZ degradation in the VL/Bi$_2$WO$_6$/PMS system. Significantly, the access of FFA (^{1}O$_2$ scavenger) can also completely quench CBZ degradation in the VL/Bi$_2$WO$_6$/PMS system, which indicates that the ^{1}O$_2$ played a key role in CBZ degradation. The generation of ^{1}O$_2$ possibly came from the transformation of •O$_2$$^-$ and PMS oxidation. However, the p-BQ (•O$_2$$^-$ scavenger) showed much less inhibition on CBZ degradation than FFA. Moreover, the •O$_2$$^-$ in the photocatalytic process might generate from the oxygen reduction by electrons, while the CBZ degradation in the VL/Bi$_2$WO$_6$/PMS system under N$_2$ purges (Figure S2) was not significantly inhibited. These results showed that ^{1}O$_2$ is likely to come from PMS oxidation rather than the •O$_2$$^-$. Thus, it was proposed that the photogenerated holes could oxidize PMS to generate SO$_5$$^{•-}$ and react with HSO$_5$$^-$ to firstly produce ^{1}O$_2$,

then produce other ROS, resulting in the key role of holes and $^1O_2$ for CBZ degradation in the VL/Bi$_2$WO$_6$/PMS system.
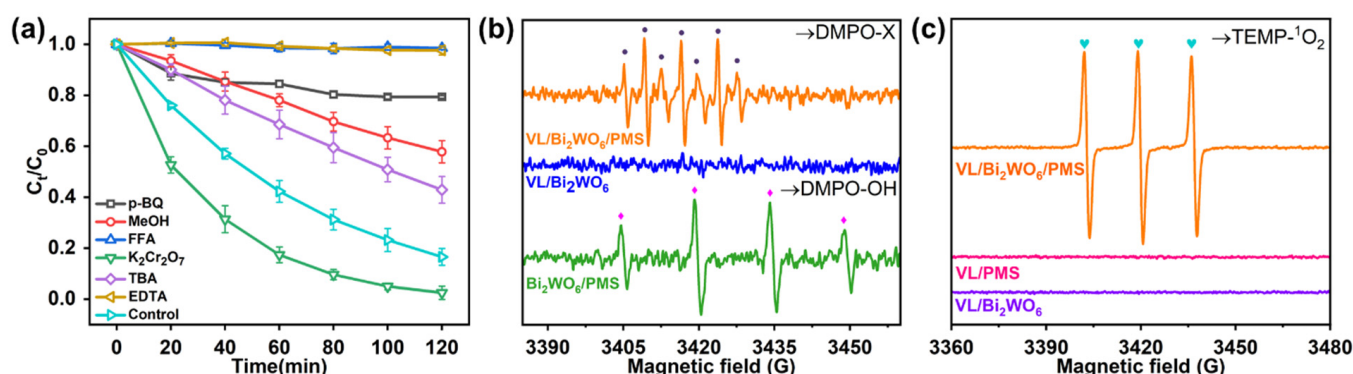

Figure 3. The quenching experiments of the VL/Bi$_2$WO$_6$/PMS process for CBZ degradation (**a**), EPR spectra by DMPO in water (**b**), EPR spectra by TEMP in water of the VL/Bi$_2$WO$_6$ and VL/Bi$_2$WO$_6$/PMS (**c**). Experimental conditions: LI = 200 mW cm^{-2}, Bi$_2$WO$_6$ dosage = 1.0 g L^{-1}, [PMS]$_0$ = 0.50 g L^{-1}, [CBZ] = 10 mg L^{-1}, pH = 7.0, T = 25 °C. p-BQ = 10 mM, MeOH = 200 mM, FFA = 20 mM, K$_2$Cr$_2$O$_7$ = 10 mM, TBA = 200 mM, EDTA = 10 mM.

To further confirm these results, the ROS was further confirmed by the EPR technique (Figure 3b). The VL/Bi$_2$WO$_6$ process found no obvious signal for its limited oxidation ability. The weak signal of ●OH peak was observed in Bi$_2$WO$_6$/PMS system, corresponding to the slight degradation of CBZ. In particular, the signal of DMPO-X was clearly observed due to the rapid oxidation of DMPO by the ROS in the VL/Bi$_2$WO$_6$/PMS system, indicating the strong oxidation capacity of the VL/Bi$_2$WO$_6$/PMS system [35]. Moreover, fairly high-intensity TEMP-$^1O_2$ signals were present in VL/Bi$_2$WO$_6$/PMS (Figure 3c), but they were not present in the VL/Bi$_2$WO$_6$ system, suggesting that the combination of Bi$_2$WO$_6$ catalyst and PMS oxidant is essential for the generation of $^1O_2$. The results further confirmed the hypothesis of the quenching experiments that the PMS was firstly oxidized by the photogenerated holes to initiate $^1O_2$ production and then generate other ROS to greatly enhance the performance of pollutant removal by the VL/Bi$_2$WO$_6$/PMS process.

2.4. Key Factors Affecting CBZ Degradation in VL/Bi$_2$WO$_6$/PMS System

Figure 4a displayed the effect of LI on CBZ degradation in the VL/Bi$_2$WO$_6$/PMS system, in which the removal rate of CBZ was found to improve with the increase in light intensity. When the LI was increased from 50 to 200 mW cm^{-2}, the degradation rate increased from 0.029 to 0.045 min^{-1}, respectively. Moreover, the removal of CBZ was slightly improved with the PMS concentration increasing from 0.20 to 1.0 g L^{-1} (Figure 4b). Furthermore, the catalyst dosage from 0.50 to 2.0 g L^{-1} induced the degradation efficacy to increase from 60% to 95% (Figure 4c). The reason for this is a large number of active sites on the surface of the catalyst. The higher the concentration of Bi$_2$WO$_6$, the better the degradation of CBZ, the more active sites of PMS, and the more radical generation. Figure 4d showed the oxidation kinetics of CBZ by VL/Bi$_2$WO$_6$/PMS process in the pH range 3.0–9.0, in which the initial pH of the CBZ had little effect on the removal of CBZ. It was indicated that the VL/Bi$_2$WO$_6$/PMS process could function in a wide pH range. From the above discussion, it can be seen that the optimal operating conditions for the VL/Bi$_2$WO$_6$/PMS process to remove pollutants are: LI is 200 mW cm^{-2}, Bi$_2$WO$_6$ is 2.0 g L^{-1}, PMS is 0.50 g L^{-1}, and the initial pH is 7.0.
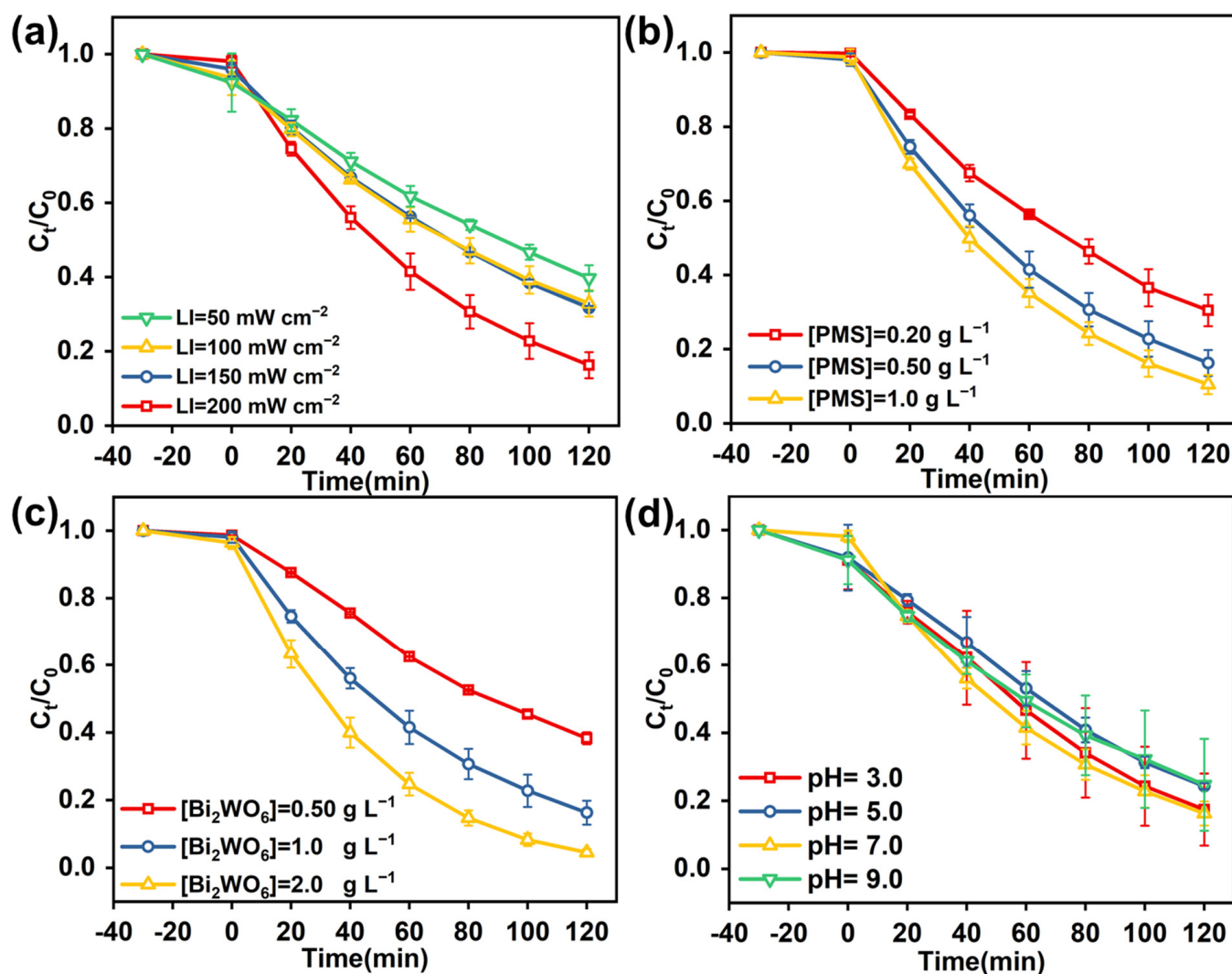
Figure 4. Effects of LI (**a**), effects of Bi_2WO_6 dosage (**b**), effects of PMS concentration (**c**), and effects of initial pH (**d**) on CBZ degradation in the $VL/Bi_2WO_6/PMS$ process. Experimental conditions: LI = 50–200 mW cm^{-2}, Bi_2WO_6 dosage = 0.50–2.0 g L^{-1}, $[PMS]_0$ = 0.20–1.0 g L^{-1}, [CBZ] = 10.0 mg L^{-1}, pH = 3.0–9.0, and T = 25 °C.

2.5. Degradation Mechanism of CBZ

In this study, the degradation pathways of CBZ were clarified by the intermediate identification and DFT calculation. To provide an in-depth verification of the $VL/Bi_2WO_6/PMS$ system for environmental remediation, the Fukui index distribution (f^0) calculated by NPA and MPA was used to predict the reaction point for radical attraction, and the results of the calculations are shown in Figure 5a and Tables 1 and 2. According to correspondent results of NPA and MPA on the highest atomic f^0 value of CBZ, 15 C and C12 is the most susceptible site, resulting in an olefinic double bond to be the preferential site for radical attack by the $VL/Bi_2WO_6/PMS$ system. The degradation intermediates were identified by LC-TOF-MS analysis and previous literature results (Table S1) [36–38]. The degradation pathway of CBZ during $VL/Bi_2WO_6/PMS$ was then elucidated on the basis of the intermediates/products detected by LC-TOF-MS (Figure 5b). Firstly, the olefin double bond was attacked by the free radical to form products A and B. Product A can be further hydroxylated to form product D or converted to its isomers to form product B. After the hydrogen rearrangement reaction, product B is converted to product C, which is then oxidized to product F, eventually forming I. Alternatively, the C-C bond of product B can be broken

to form the bis-formaldehyde product E, which can then undergo ring closure to produce product G. Then, the aldehyde group on product G can be oxidized to a carboxyl group and further lost to form product H. In addition, the oxidation of product H produces product I. Product I (acridine) is reported to be one of the most common photodegradation products of CBZ [39]. During the reaction, product H and product I can further open the ring to form product J. Thus, the CBZ degradation pathway was proposed by the combination of the experimental assay with the theoretical predictions.
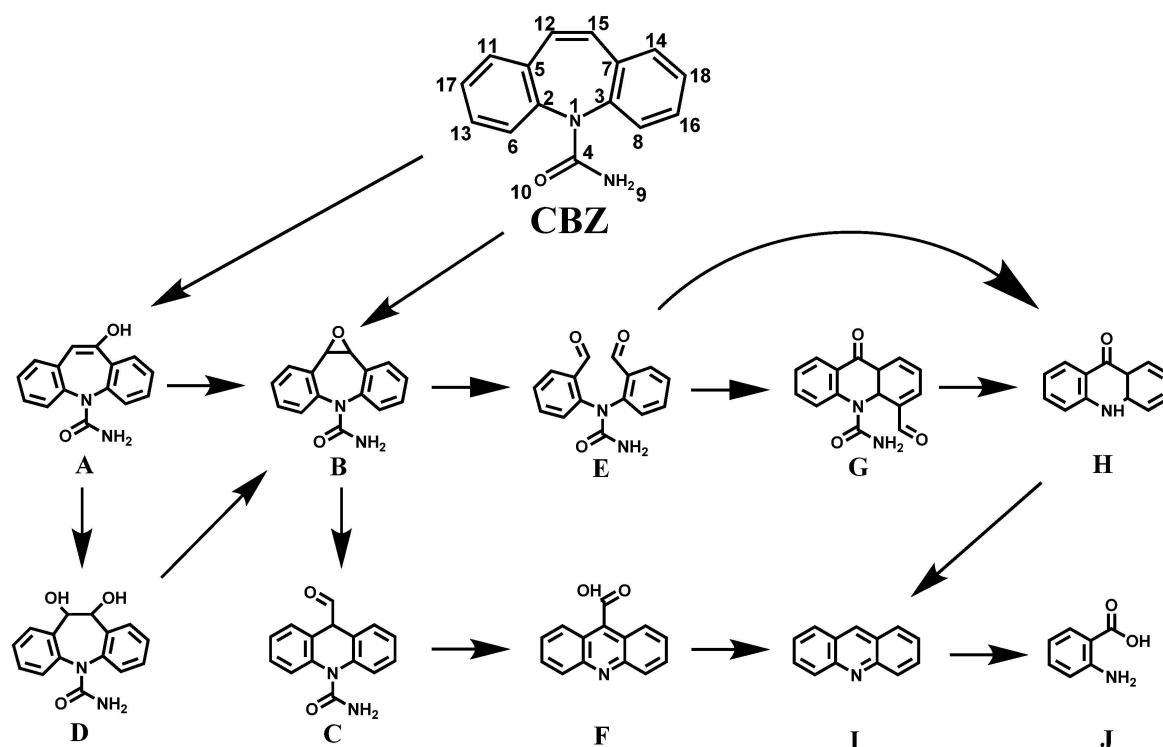

Figure 5. The suggested degradation pathway of CBZ by Bi_2WO_6 under visible light irradiation (The detail of product A–J was displayed in Table S1).

Table 1. Condensed Fukui index (f^0) distribution by NPA on CBZ.

Num.	Atom	N	N + 1	N − 1	f^0
1	N	−0.519	−0.512	−0.379	0.066
2	C	0.165	0.110	0.223	0.056
3	C	0.141	0.081	0.223	0.071
4	C	0.828	0.822	0.823	0.000
5	C	−0.090	−0.112	−0.073	0.019
6	C	−0.238	−0.252	−0.263	−0.006
7	C	−0.085	−0.114	−0.067	0.024
8	C	−0.243	−0.255	−0.263	−0.004
9	N	−0.895	−0.903	−0.827	0.038
10	O	−0.781	−0.800	−0.658	0.071
11	C	−0.220	−0.273	−0.195	0.039
12	C	−0.222	−0.350	−0.146	0.102
13	C	−0.247	−0.339	−0.186	0.076
14	C	−0.219	−0.272	−0.195	0.039
15	C	−0.228	−0.350	−0.165	0.092
16	C	−0.246	−0.344	−0.186	0.079
17	C	−0.251	−0.271	−0.218	0.027
18	C	−0.247	−0.270	−0.217	0.026

Table 2. Condensed Fukui index (f^0) distribution by MPA on CBZ.

Num.	Atom	N	N + 1	N − 1	f^0
1	N	0.184	0.034	0.176	−0.071
2	C	−1.109	−0.806	−0.739	−0.033
3	C	−1.100	−0.928	−0.736	−0.096
4	C	0.855	0.805	0.293	0.256
5	C	0.683	0.199	0.902	−0.352
6	C	0.348	0.179	0.216	−0.018
7	C	0.657	0.051	0.902	−0.425
8	C	0.331	0.186	0.214	−0.014
9	N	0.149	0.132	0.307	−0.088
10	O	−0.660	−0.675	−0.474	−0.100
11	C	−0.095	−0.024	0.391	−0.207
12	C	−0.090	0.078	−0.341	0.210
13	C	0.037	−0.087	−0.140	0.026
14	C	−0.083	−0.016	0.392	−0.204
15	C	−0.100	0.046	−0.340	0.193
16	C	−0.073	−0.175	−0.141	−0.017
17	C	0.017	−0.026	0.059	−0.043
18	C	0.050	0.026	0.059	−0.017

Acute toxicity, developmental toxicity, and bioaccumulation factors of phenanthrene and its degradation intermediates/products were assessed using Toxicity Estimation Software (T.E.S.T.) based on quantitative structure-activity relationship (QSAR) prediction. As shown in Figure 6a, the LD_{50} of CBZ in rats is 1807 mg/kg, which is considered "toxic". The LD_{50} of almost all degradation intermediates was higher than that of CBZ (except intermediates H), indicating reduced acute toxicity of the intermediates especially intermediates B, D, and J. Figure 6b showed that the photocatalytic degradation process could reduce its bioconcentration factor compared to the original CBZ. It is noteworthy that the bioconcentration factors of both product I and product H are higher than those of CBZ. Moreover, CBZ is a "developmental toxicant", while the treatment process reduces the toxicity of some of the degradation intermediates, and intermediates J and I are even "developmentally non-toxicant". The CBZ was calculated to be "mutagenicity positive", while the mutagenicity of the intermediates was reduced to "mutagenicity negative" during the photocatalytic treatment. However, only half of the products were reduced to "mutagenicity negative", while the rest were still "mutagenicity positive". From the calculations, it appears that the degradation process can reduce CBZ toxicity, but most intermediates are still toxic, which needs mentioning.

2.6. Possible Mechanism of CBZ Degradation by VL/Bi₂WO₆/PMS System

Based on the experimental analysis and theoretical prediction, Scheme 1 proposes the overall possible mechanism of CBZ oxidation by VL/Bi_2WO_6/PMS system. When PMS is added to the photocatalysis of Bi_2WO_6 materials under visible light, CBZ degradation can be effectively promoted. The PMS was first oxidized by the light-generated holes, which initiated the production of $^1O_2$ and then the other ROS, greatly enhancing the pollutant removal capacity of the VL/Bi_2WO_6/PMS system. The generation of these radicals follows Equations (1)–(10). Furthermore, the VL/Bi_2WO_6/PMS system prefers to attack the 12 C and 15 C atoms on CBZ, leading to the oxidation of the C=C bond, thus breaking down CBZ into lower molecules. From the calculations, it appears that the degradation process can reduce the toxicity of CBZ, but most of the intermediates are still toxic to be mentioned.
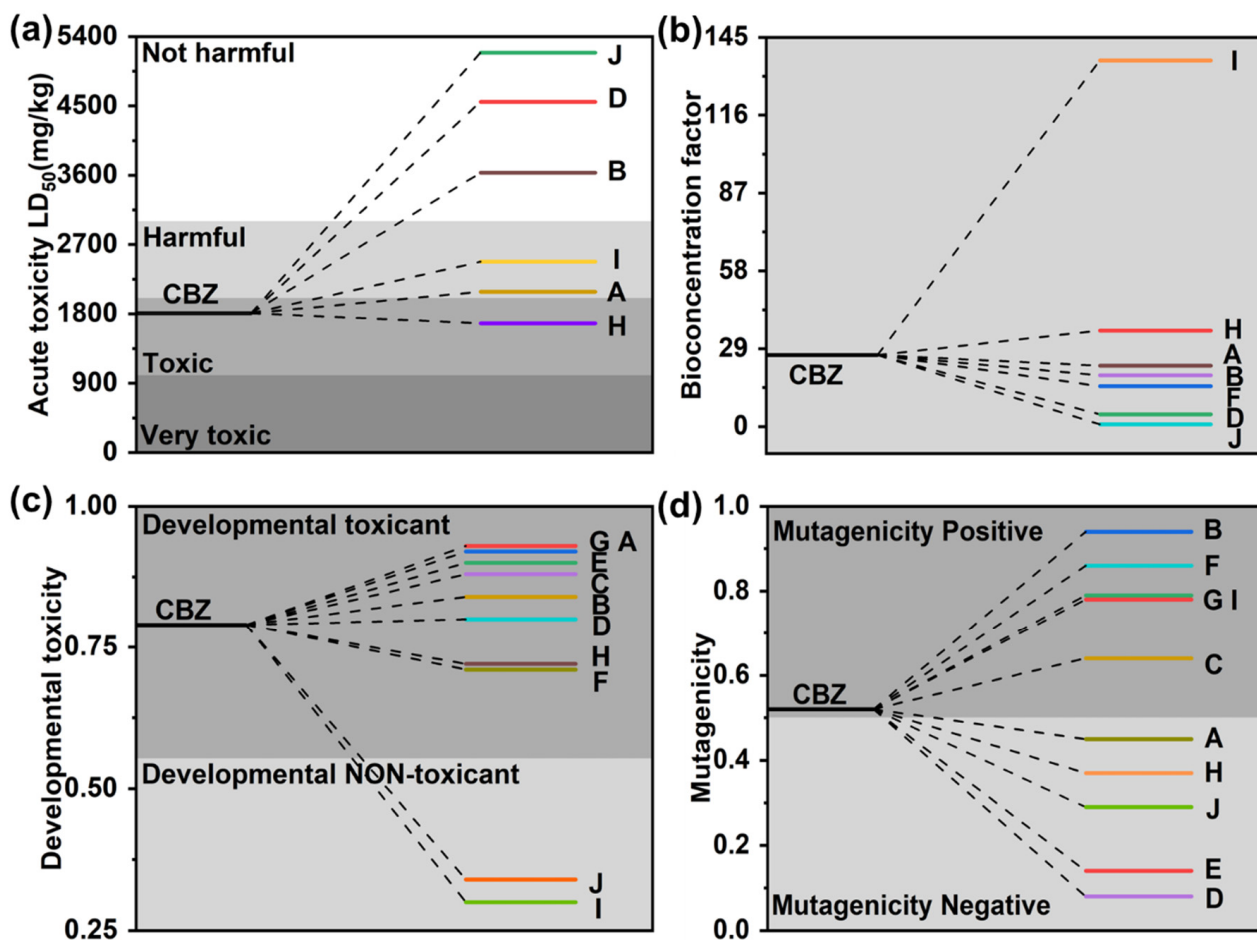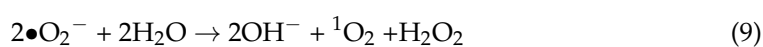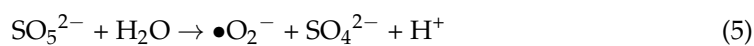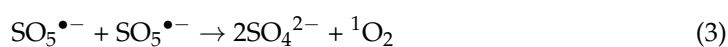
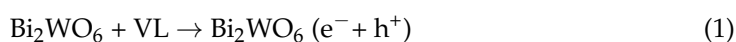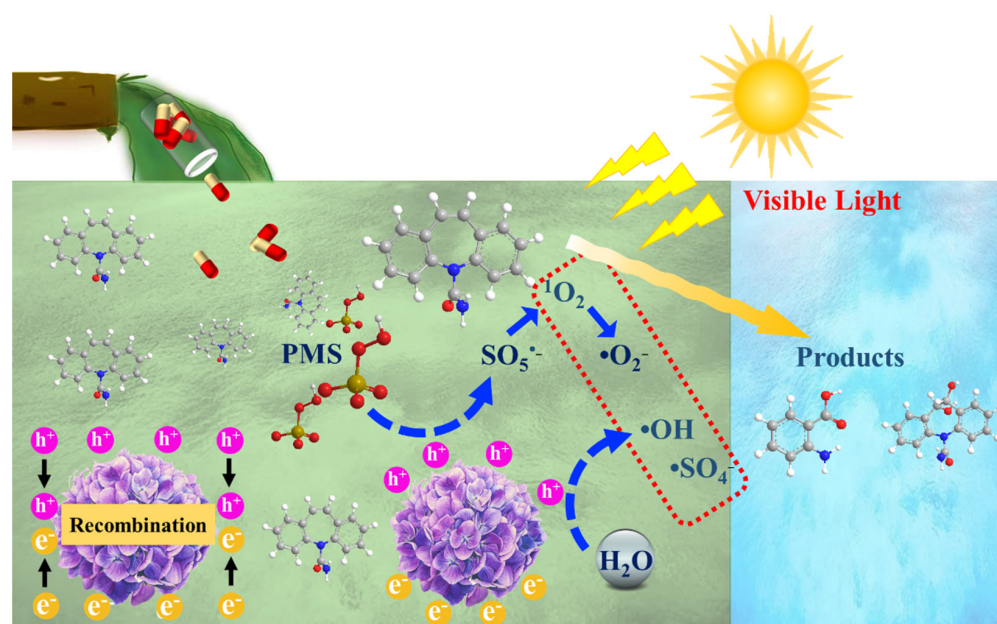**Figure 6.** (**a**) Acute toxicity, (**b**) bioconcentration factor, (**c**) developmental toxicity, and (**d**) mutagenicity of CBZ and degradation intermediates.

$$Bi_2WO_6 + VL \rightarrow Bi_2WO_6\ (e^- + h^+) \tag{1}$$

$$HSO_5^- + h^+ \rightarrow SO_5^{\bullet-} + H^+ \tag{2}$$

$$SO_5^{\bullet-} + SO_5^{\bullet-} \rightarrow 2SO_4^{2-} + {}^1O_2 \tag{3}$$

$$HSO_5^- \rightarrow H^+ + SO_5^{2-} \tag{4}$$

$$SO_5^{2-} + H_2O \rightarrow \bullet O_2^- + SO_4^{2-} + H^+ \tag{5}$$

$$H_2O + h^+ \rightarrow \bullet OH + H^+ \tag{6}$$

$$HSO_5^- + \bullet OH \rightarrow SO_4^{\bullet-} + OH^- \tag{7}$$

$$SO_4^{\bullet-} + OH^- \rightarrow SO_4^{2-} + \bullet OH \tag{8}$$

$$2\bullet O_2^- + 2H_2O \rightarrow 2OH^- + {}^1O_2 + H_2O_2 \tag{9}$$

$$\bullet O_2^- + \bullet OH \rightarrow {}^1O_2 + OH^- \tag{10}$$

Scheme 1. Proposed mechanism of the VL/Bi_2WO_6/PMS process on the oxidation of CBZ.

3. Materials and Methods

3.1. Chemicals

Carbamazepine (CBZ), 5,5-dimethyl-1-pyrroline (DMPO), and PMS ($KHSO_5$) were obtained from Sigma-Aldrich and used as recipients. The raw materials of sodium tungstate ($Na_2WO_4 \bullet 2H_2O$) and 1,4-benzoquinone (p-BQ) were purchased from Macklin. Tert-butanol (TBA), furfuryl alcohol (FFA), and bismuth nitrate ($Bi(NO_3)_3 \bullet 5H_2O$) were purchased from Aladdin. HPLC grade of formic acid and methanol (MeOH) were purchased from Oceanpak and Anpel Laboratory Technologies (Shanghai) Inc., Shanghai, China. The chemical reagents in this study were not treated in any step prior to use.

3.2. Synthesis and Characterization of Bi_2WO_6

Bi_2WO_6 was prepared with reference to a previous study [40]. In detail, a hydrothermal reaction scheme was used to synthesize Bi_2WO_6. First of all, 10 mmol $Bi(NO_3)_3 \bullet 5H_2O$ was dissolved in 25 mL of distilled water and stirred well to designate solution I. Additional solution II was prepared by dissolving 10 mmol of $Na_2WO_4 \bullet 2H_2O$ in distilled water and mixing by sonication. After dropping into solution I, solution II was added drop by drop under sonication. The resultant slurry was magnetically stirred for 1 h and processed hydrothermally in two 50 mL Teflon-lined stainless steel autoclaves at 160 °C for 12 h. After reactions, the white product was centrifuged at 5000 rpm and washed twice with alternating ethanol and deionized water. Lastly, the collected products were dried in an oven at 80 °C. The resulting Bi_2WO_6 material was then characterized. The microstructural characteristics of the Bi_2WO_6 were observed by X-ray diffraction (XRD) via a monochromatic Cu Kα radiation (λ = 1.5406Å), 2θ = 20°–80° (Ulitma IV, Rigaku, Tokyo, Japan). The morphology of Bi_2WO_6 was observed by field emission scanning electron microscopy (SEM) (EVO MA 15, ZEISS, Jena, Germany) and transmission electron microscopy (TEM) (Talos F200S, FEI, Waltham, MA, USA). X-ray photoelectron spectroscopy (XPS) analysis was performed on a K-Alpha instrument (Thermo Fisher, Waltham, MA, USA).

3.3. Experiment Procedures

The photocatalytic experiments were conducted under visible light irradiation through a Xenon lamp (PLS-SXE300+, Beijing Perfectlight Technology Co., Ltd., Beijing, China). During this experiment, Bi_2WO_6 with a concentration of 1.0 g L^{-1} was added to a glass vial containing 20 mL of solution with 10.0 mg L^{-1} of CBZ. Mean light intensity (LI) was

tuned at 200 mW cm^{-2}, the PMS concentration was set at 0.50 g L^{-1}, while the pH of the reaction solution was adjusted at 7.0 $\pm$ 0.05. All runs were conducted in duplicate, while the average value was used to guarantee reproducible results. For a certain time step, the reaction sample (0.80 mL) was extracted and directly filtered in a flask for LC analyses (UHPLC, Dionex UltiMate 3000, Thermo Scientific, USA).

3.4. Analytic and Theoretical Methods

CBZ concentrations were analyzed by a DIONEX UltiMate 3000 using a Phenomenex Kinetex ×®Phenyl-Hexyl 100Å column (2.1 mm × 50 mm, 2.6 μm). The intermediate product of CBZ was determined by using LC-TOF-MS (UPLC 1290-6540B Q-TOF) after solid-phase extraction (Text S1). In the mobile phase, acetonitrile and 0.1% formic acid were mixed in a 40:60 volume ratio, and the injection volume of the sample was 10 μL. Mass spectrometry was performed under ESI+ in the mass range of 50–500 *m/z*.

The rapid development of computational chemistry makes it possible to predict the reactive sites of a relatively large molecule, such as CBZ. DFT is one of the best methods to realize familiar chemical concepts such as electronegativity, electron affinity, ionization potential, chemical potential, etc. The Fukui function is a popular tool for predicting the regioselectivity in a radical-involved reaction. Through proper visualization, the Fukui function can roughly exhibit the regioselectivity of CBZ [41]. Specifically, an atom surrounded by a larger positive function isosurface means it is more active. Furthermore, the calculation of Mulliken's atomic charge of a molecule or complex has a vital role in the application of chemical calculations since atomic charges affect the physical properties such as molecular polarizability, dipole moment, electronic structure, and other various properties of a molecular system. However, the natural analysis is an alternative to the conventional Mulliken population analysis. It seems to reveal numerical stability and to better explain the electron distribution in a molecule. The charge distribution on the atom reveals the formation of pairs of donor and acceptor, which can involve the charge transfer in the molecule [42]. To make reactive site prediction easier to read, the individual atomic charge calculated by NPA (Natural Population Analysis) and MPA (Mulliken Population Analysis) has been used to calculate the Fukui descriptor of reactivity according to Equations (11)–(14). [43] The larger value of the Fukui function, the higher reactivity of the corresponding site. Specifically, Fukui function is defined as:

$$f(r) = \left(\frac{\partial^2 E}{\partial N. \, \partial v(r)} \right) = \left[\frac{\partial \mu}{\partial v(r)} \right]_N = \left[\frac{\partial \rho(r)}{\partial N} \right]_{V(r)} \tag{11}$$

where $\rho(r)$ is the electron density at a point r in space, N is the electron number in the present system, and the constant term v in the partial derivative is external potential. The Fukui function per atom in a molecule is defined as follows:

$$f^+(r) = [q(N + 1) - q(N)] \tag{12}$$

$$f^-(r) = [q(N) - q(N - 1)] \tag{13}$$

$$f^0(r) = \frac{f^+(r) - f^-(r)}{2} \tag{14}$$

q is the total number of electrons in an atom in a molecule. Specifically, f^+ and f^- respectively represent the reaction potential for nucleophilic and electrophilic attack, while f^0 responds to radical attack. The geometry optimization of CBZ was simulated by the DFT with Gaussian 09 package, using the method of B3LYP/6-31+G** combined with the SMD solvent model [37,44].

4. Conclusions

Previous studies usually adopt PMS as the electron acceptor in the photocatalytic process, in which the effect and contribution of holes for PMS activation were overlooked. However, the efficient utilization of holes plays an important role in taking full advantage of the sunlight resource. Thus this study takes a new insight into the effect of holes in PMS activation for pollutants removal. The results indicate that holes could firstly oxidize PMS to initiate the generation of $^1O_2$ and then induce the production of other ROS, resulting in the efficient removal of pollutants. The discussion also confirms that the holes can adopt PMS as the electron donor to enhance the capacity of photocatalysis. Therefore, this study provides an avenue to improve efficiency and widen the application of photocatalytic technologies. Moreover, it is worth noting that the products produced by photocatalytic degradation of CBZ may exhibit greater toxicity than the parent based on quantitative structure-activity relationship prediction calculations, which warn future treatment technologies to pay more attention to the safe treatment of organics.

Supplementary Materials: The following supporting information can be downloaded at: https://www.mdpi.com/article/10.3390/catal12111327/s1, Text S1: Methods of solid phase extraction; Table S1: Compounds identified by LC-MS during the photocatalytic degradation of CBZ under visible light irradiation; Figure S1: Survey XPS spectrum of the Bi2WO6 sample; Figure S2: The degradation of CBZ in the VL/Bi2WO6/PMS system under N2 purge.

Author Contributions: Conceptualization, R.Y.; methodology, Y.Q. and X.Z.; software, W.G.; validation, Z.L.; writing—original draft preparation, Y.Q. and R.Y.; writing—review and editing, A.J.L., J.Q. and H.L.; supervision, A.J.L.; project administration, R.Q.; funding acquisition, R.Y. and A.J.L. All authors have read and agreed to the published version of the manuscript.

Conflicts of Interest: The authors declare that they have no known competing financial interests or personal relationships that could have appeared to influence the work reported in this paper.

References

1. Xu, S.; Gao, X.; Xu, W.; Jin, P.; Kuang, Y. Efficient photocatalytic degradation of commercial pharmaceutical contaminants of carbamazepine using BiOBr nanosheets under visible-light irradiation. *Mater. Sci. Semicond. Process.* **2022**, *137*, 106207. [CrossRef]
2. Zhou, Z.; Wu, Y.; Xu, Y.; Wang, Z.; Fu, H.; Zheng, Y. Carbamazepine degradation and genome sequencing of a novel exoelectrogen isolated from microbial fuel cells. *Sci. Total Environ.* **2022**, *838*, 156161. [CrossRef] [PubMed]
3. Shafiq, I.; Hussain, M.; Shafique, S.; Rashid, R.; Akhter, P.; Ahmed, A.; Jeon, J.; Park, Y. Oxidative desulfurization of refinery diesel pool fractions using LaVO$_4$ photocatalyst. *J. Ind. Eng. Chem.* **2021**, *98*, 283–288. [CrossRef]
4. Yang, Y.; Feng, H.; Niu, C.; Huang, D.; Guo, H.; Liang, C.; Liu, H.; Chen, S.; Tang, N.; Li, L. Constructing a plasma-based Schottky heterojunction for near-infrared-driven photothermal synergistic water disinfection: Synergetic effects and antibacterial mechanisms. *Chem. Eng. J.* **2021**, *426*, 131902. [CrossRef]
5. Mahboob, I.; Shafiq, I.; Shafique, S.; Akhter, P.; Amjad, U.; Hussain, M.; Park, Y. Effect of active species scavengers in photocatalytic desulfurization of hydrocracker diesel using mesoporous Ag$_3$VO$_4$. *Chem. Eng. J.* **2022**, *441*, 136063. [CrossRef]
6. Lin, Y.; Zhang, Y.; Li, G. Promotion of sulfameter degradation by coupling persulfate and photocatalytic advanced oxidation processes with Fe-doped MOFs. *Sep. Purif. Technol.* **2022**, *282*, 119632. [CrossRef]
7. Azalok, K.A.; Oladipo, A.A.; Gazi, M. UV-light-induced photocatalytic performance of reusable MnFe-LDO–biochar for tetracycline removal in water. *J. Photoch. Photobiol. A* **2021**, *405*, 112976. [CrossRef]
8. Yin, R.; Jing, B.; He, S.; Hu, J.; Lu, G.; Ao, Z.; Wang, C.; Zhu, M. Near-infrared light to heat conversion in peroxydisulfate activation with MoS$_2$: A new photo-activation process for water treatment. *Water Res.* **2021**, *190*, 116720. [CrossRef]
9. Yin, R.L.; Chen, Y.X.; Hu, J.Y.; Lu, G.; Zeng, L.X.; Choi, W.Y.; Zhu, M.S. Complexes of Fe(III)-organic pollutants that directly activate Fenton-like processes under visible light. *Appl. Catal. B* **2021**, *283*, 119663. [CrossRef]
10. Kisch, H. Semiconductor photocatalysis for chemoselective radical coupling reactions. *Acc. Chem. Res.* **2017**, *50*, 1002–1010. [CrossRef]
11. Li, J.D.; Fang, W.; Yu, C.L.; Zhou, W.Q.; Zhu, L.H.; Xie, Y. Ag-based semiconductor photocatalysts in environmental purification. *Appl. Surf. Sci.* **2015**, *358*, 46–56. [CrossRef]

12. Xiang, Q.; Cheng, F.; Lang, D. Hierarchical layered WS$_2$/graphene-modified CdS nanorods for efficient photocatalytic hydrogen evolution. *ChemSusChem* **2016**, *9*, 996–1002. [CrossRef]

13. Liu, X.; Gu, S.; Zhao, Y.; Zhou, G.; Li, W. BiVO$_4$, Bi$_2$WO$_6$ and Bi$_2$MoO$_6$ photocatalysis: A brief review. *J. Mater. Sci. Technol.* **2020**, *56*, 45–68. [CrossRef]

14. Yu, S.; Zhang, Y.; Li, M.; Du, X.; Huang, H. Non-noble metal Bi deposition by utilizing Bi$_2$WO$_6$ as the self-sacrificing template for enhancing visible light photocatalytic activity. *Appl. Surf. Sci.* **2017**, *391*, 491–498. [CrossRef]

15. Liang, W.; Pan, J.; Duan, X.; Tang, H.; Xu, J.; Tang, G. Biomass carbon modified flower-like Bi$_2$WO$_6$ hierarchical architecture with improved photocatalytic performance. *Ceram. Int.* **2020**, *46*, 3623–3630. [CrossRef]

16. Wang, Q.; He, J.; Shi, Y.; Zhang, S.; Niu, T.; She, H.; Bi, Y. Designing non-noble/semiconductor Bi/BiVO$_4$ photoelectrode for the enhanced photoelectrochemical performance. *Chem. Eng. J.* **2017**, *326*, 411–418. [CrossRef]

17. Zhang, X.; Zhang, M.; Cao, K. Hydrothermal synthesis of Sm-doped Bi$_2$WO$_6$ flower-like microspheres for photocatalytic degradation of rhodamine B. *CrystEngComm* **2019**, *21*, 6208–6218. [CrossRef]

18. Wu, C.; Zhong, J.; Xie, J.; Wang, D.; Shi, Y.; Chen, Q.; Yan, H.; Zhu, J. Enhanced visible-light-driven photocatalytic properties of acceptor dopant Nb^{5+} modified Bi$_2$WO$_6$ by tailoring the morphology from 3D hierarchical microspheres to 2D nanosheets. *Appl. Surf. Sci.* **2019**, *484*, 112–123. [CrossRef]

19. Bai, Y.; Mao, W.; Wu, Y.; Gao, Y.; Wang, T.; Liu, S. Synthesis of novel ternary heterojunctions via Bi$_2$WO$_6$ coupling with CuS and g-C$_3$N$_4$ for the highly efficient visible-light photodegradation of ciprofloxacin in wastewater. *Colloid. Surf. A* **2021**, *610*, 125481. [CrossRef]

20. Orimolade, B.O.; Idris, A.O.; Feleni, U.; Mamba, B. Recent advances in degradation of pharmaceuticals using Bi$_2$WO$_6$ mediated photocatalysis-A comprehensive review. *Environ. Pollut.* **2021**, *289*, 117891. [CrossRef]

21. Ding, X.; Zhao, K.; Zhang, L. Enhanced Photocatalytic Removal of Sodium Pentachlorophenate with self-doped Bi$_2$WO$_6$ under visible light by generating more superoxide ions. *Environ. Sci. Technol.* **2014**, *48*, 5823–5831. [CrossRef] [PubMed]

22. Qamar, M.; Elsayed, R.B.; Alhooshani, K.R.; Ahmed, M.I.; Bahemann, D.W. Highly efficient and selective oxidation of aromatic alcohols photocatalyzed by nanoporous hierarchical Pt/Bi$_2$WO$_6$ in organic solvent-free environment. *ACS Appl. Mater. Inter.* **2015**, *7*, 1257–1269. [CrossRef] [PubMed]

23. Lu, X.; Che, W.; Hu, X.; Wang, Y.; Zhang, A.; Deng, F.; Luo, S.; Dionysiou, D.D. The facile fabrication of novel visible-light-driven Z-scheme CuInS$_2$/Bi$_2$WO$_6$ heterojunction with intimate interface contact by in situ hydrothermal growth strategy for extraordinary photocatalytic performance. *Chem. Eng. J.* **2019**, *356*, 819–829. [CrossRef]

24. Xue, W.; Peng, Z.; Huang, D.; Zeng, G.; Wen, X.; Deng, R.; Yang, Y.; Yan, X. In situ synthesis of visible-light-driven Z-scheme AgI/Bi$_2$WO$_6$ heterojunction photocatalysts with enhanced photocatalytic activity. *Ceram. Int.* **2019**, *45*, 6340–6349. [CrossRef]

25. Yin, R.; Chen, Y.; Hu, J.; Jin, S.; Guo, W.; Zhu, M. Peroxydisulfate bridged photocatalysis of covalent triazine framework for carbamazepine degradation. *Chem. Eng. J.* **2022**, *427*, 131613. [CrossRef]

26. Xiao, Z.; Feng, X.; Shi, H.; Zhou, B.; Wang, W.; Ren, N. Why the cooperation of radical and non-radical pathways in PMS system leads to a higher efficiency than a single pathway in tetracycline degradation. *J. Hazard. Mater.* **2022**, *424*, 127247. [CrossRef]

27. Guo, H.; Niu, H.; Liang, C.; Niu, C.; Liu, Y.; Tang, N.; Yang, Y.; Liu, H.; Yang, Y.; Wang, W. Few-layer graphitic carbon nitride nanosheet with controllable functionalization as an effective metal-free activator for peroxymonosulfate photocatalytic activation: Role of the energy band bending. *Chem. Eng. J.* **2020**, *401*, 126072. [CrossRef]

28. Yin, R.; Guo, W.; Wang, H.; Du, J.; Zhou, X.; Wu, Q.; Zheng, H.; Chang, J.; Ren, N. Enhanced peroxymonosulfate activation for sulfamethazine degradation by ultrasound irradiation: Performances and mechanisms. *Chem. Eng. J.* **2018**, *335*, 145–153. [CrossRef]

29. Peng, J.; Wang, Z.; Wang, S.; Liu, J.; Zhang, Y.; Wang, B.; Gong, Z.; Wang, M.; Dong, H.; Shi, J.; et al. Enhanced removal of methylparaben mediated by cobalt/carbon nanotubes (Co/CNTs) activated peroxymonosulfate in chloride-containing water: Reaction kinetics, mechanisms and pathways. *Chem. Eng. J.* **2021**, *409*, 128176. [CrossRef]

30. Qi, C.; Wen, Y.; Zhao, Y.; Dai, Y.; Li, Y.; Xu, C.; Yang, S.; He, H. Enhanced degradation of organic contaminants by Fe(III)/peroxymonosulfate process with l-cysteine. *Chin. Chem. Lett.* **2022**, *33*, 2125–2128. [CrossRef]

31. Peng, Y.; Tang, H.; Yao, B.; Gao, X.; Yang, X.; Zhou, Y. Activation of peroxymonosulfate (PMS) by spinel ferrite and their composites in degradation of organic pollutants: A review. *Chem. Eng. J.* **2021**, *414*, 128800. [CrossRef]

32. Dai, Y.; Qi, C.; Cao, H.; Wen, Y.; Zhao, Y.; Xu, C.; Yang, S.; He, H. Enhanced degradation of sulfamethoxazole by microwave-activated peracetic acid under alkaline condition: Influencing factors and mechanism. *Sep. Purif. Technol.* **2022**, *288*, 120716. [CrossRef]

33. Li, C.; Sun, T.; Yi, G.; Zhang, D.; Zhang, Y.; Lin, X.; Liu, J.; Shi, Z.; Lin, Q. Fabrication of a Ag/CNQDs/g-C$_3$N$_4$-PVDF photocatalytic composite membrane with excellent photocatalytic and self-cleaning properties. *J. Environ. Chem. Eng.* **2022**, *10*, 108488. [CrossRef]

34. Dai, Y.; Cao, H.; Qi, C.; Zhao, Y.; Wen, Y.; Xu, C.; Zhong, Q.; Sun, D.; Zhou, S.; Yang, B.; et al. L-cysteine boosted Fe(III)-activated peracetic acid system for sulfamethoxazole degradation: Role of L-cysteine and mechanism. *Chem. Eng. J.* **2023**, *451*, 138588. [CrossRef]

35. Tian, N.; Tian, X.; Nie, Y.; Yang, C.; Zhou, Z.; Li, Y. Enhanced 2, 4-dichlorophenol degradation at pH 3-11 by peroxymonosulfate via controlling the reactive oxygen species over Ce substituted 3D Mn$_2$O$_3$. *Chem. Eng. J.* **2019**, *355*, 448–456. [CrossRef]

36. Dong, H.; Chen, J.; Feng, L.; Zhang, W.; Guan, X.; Strathmann, T.J. Degradation of organic contaminants through activating bisulfite by cerium (IV): A sulfate radical-predominant oxidation process. *Chem. Eng. J.* **2019**, *357*, 328–336. [CrossRef]

37. Zhao, C.; Liao, Z.; Liu, W.; Liu, F.; Ye, J.; Liang, J.; Li, Y. Carbon quantum dots modified tubular g-C_3N_4 with enhanced photocatalytic activity for carbamazepine elimination: Mechanisms, degradation pathway and DFT calculation. *J. Hazard. Mater.* **2020**, *381*, 120957. [CrossRef]

38. Yang, L.; Hao, X.; Yu, D.; Zhou, P.; Peng, Y.; Jia, Y.; Zhao, C.; He, J.; Zhan, C.; Lai, B. High visible-light catalytic activity of Bis-PDI-T@TiO_2 for activating persulfate toward efficient degradation of carbamazepine. *Sep. Purif. Technol.* **2021**, *263*, 118384. [CrossRef]

39. Duan, Y.; Deng, L.; Shi, Z.; Zhu, L.; Li, G. Assembly of graphene on Ag_3PO_4/AgI for effective degradation of carbamazepine under Visible-light irradiation: Mechanism and degradation pathways. *Chem. Eng. J.* **2019**, *359*, 1379–1390. [CrossRef]

40. Xu, X.; Xiao, L.; Wu, Z.; Jia, Y.; Ye, X.; Wang, F.; Yuan, B.; Yu, Y.; Huang, H.; Zou, G. Harvesting vibration energy to piezo-catalytically generate hydrogen through Bi_2WO_6 layered-perovskite. *Nano Energy* **2020**, *78*, 105351. [CrossRef]

41. Li, Y.; Yang, Y.; Lei, J.; Liu, W.; Tong, M.; Liang, J. The degradation pathways of carbamazepine in advanced oxidation process: A mini review coupled with DFT calculation. *Sci. Total Environ.* **2021**, *779*, 146498. [CrossRef] [PubMed]

42. Isravel, A.D.; Jeyaraj, J.K.; Thangasamy, S.; John, W.J. DFT, NBO, HOMO-LUMO, NCI, stability, Fukui function and hole–Electron analyses of tolcapone. *Comput. Theor. Chem.* **2021**, *1202*, 113296. [CrossRef]

43. Gurkan, Y.Y.; Turkten, N.; Hatipoglu, A.; Cinar, Z. Photocatalytic degradation of cefazolin over N-doped TiO_2 under UV and sunlight irradiation: Prediction of the reaction paths via conceptual DFT. *Chem. Eng. J.* **2012**, *184*, 113–124. [CrossRef]

44. Wang, K.; Yang, L.; Wang, X.; Guo, L.; Cheng, G.; Zhang, C.; Jin, S.; Tan, B.; Cooper, A. Covalent triazine frameworks via a low-temperature polycondensation approach. *Angew. Chem. Int. Ed.* **2017**, *56*, 14149–14153. [CrossRef] [PubMed]